



TECHNICAL REPORT 3060  
March 2016

**Evaluation of Characteristic Energy  
Scales of Pressure Stabilized Oxygen  
Chain States in  $\text{YBa}_2\text{Cu}_3\text{O}_{7-x}$  Films**

Benjamin J. Taylor  
Teresa Emery-Adleman

Approved for public release.

SSC Pacific  
San Diego, CA 92152-5001

**SSC Pacific**  
**San Diego, California 92152-5001**

---

**G. M. Bonitz, CAPT, USN**  
Commanding Officer

**C. A. Keeney**  
Executive Director

**ADMINISTRATIVE INFORMATION**

The work described in this report was performed by the Advanced Concepts and Applied Research Branch (Code 71730) of the Advanced Systems and Applied Sciences Division (Code 71700), Space and Naval Warfare Systems Center Pacific (SSC Pacific), San Diego, CA. The SSC Pacific Naval Innovative Science and Engineering (NISE) Program provided funding for this Basic Applied Research project.

Released by  
Joanna N. Ptasinski, Head  
Advanced Concepts and Applied Research  
Branch

Under authority of  
Ayax Ramirez, Head  
Advanced Systems and Applied  
Sciences Division

This is a work of the United States Government and therefore is not copyrighted. This work may be copied and disseminated without restriction.

## EXECUTIVE SUMMARY

Over the past decade key experiments have been performed by a number of authors on the evolution of characteristic physical properties of the high- $T_c$  compound  $\text{YBa}_2\text{Cu}_3\text{O}_x$ . By using the now available reported values of the critical temperature,  $T_c$ , the upper critical field,  $H_{c2}(0)$ , the superconducting effective mass,  $m^*$ , and the superconducting penetration depth,  $\lambda$ , we examine the nature of characteristic energy scales of pressure stabilized “quantum structural” lattice states in  $\text{YBa}_2\text{Cu}_3\text{O}_{\nabla x}$  films.

# CONTENTS

<b>EXECUTIVE SUMMARY .....</b>	<b>iii</b>
<b>1. INTRODUCTION.....</b>	<b>1</b>
<b>2. GEOMETRY OF THERMAL GRADIENT ANNEALING.....</b>	<b>2</b>
<b>3. FUNDIMENTAL PHYSICAL PROPERTIES OF <math>\text{YBa}_2\text{Cu}_3\text{O}_x</math> vs. HOLE DOPING .....</b>	<b>5</b>
<b>4. SUPERCONDUCTIVITY AND ORDERED LATTICE STATES.....</b>	<b>9</b>
<b>5. CONCLUSION .....</b>	<b>14</b>
<b>REFERENCES.....</b>	<b>15</b>

## Figures

1. Depiction of the annealing device developed for the preparation of $\text{YBa}_2\text{Cu}_3\text{O}_{\nabla x}$ films ....	1
2. Example showing the conduit for the thermal heat path between the heat source and the heat sink parallel to the substrate/film interface .....	4
3. Relationship between the oxygen doping content, $\text{O}_x$ , and the hole doping value, $p(\text{h/Cu})$ , in the Cu-O <sub>2</sub> planes .....	6
4. The superconducting penetration depth $\lambda$ vs. $p$ of the $\text{YBa}_2\text{Cu}_3\text{O}_x$ system.....	7
5. The superconducting effective mass $m^*$ vs. $p$ of the $\text{YBa}_2\text{Cu}_3\text{O}_x$ system as determined from optical conductivity measurements.....	8
6. Upper critical field, $H_{c2}(0)$ , of the hole-doped cuprates $\text{YBa}_2\text{Cu}_3\text{O}_x$ and $\text{Tl}_2\text{Ba}_2\text{CuO}_{6+\delta}$ ...	11
7. Calculated ratio of the normal state carrier density to the superconducting state carrier density $\frac{n_n}{n_s}$ vs. $p$ for the $\text{YBa}_2\text{Cu}_3\text{O}_x$ system.....	12
8. Quantized Ratios.....	13

# 1. INTRODUCTION

We have recently developed a sample preparation method wherein the resulting film has a monotonically varying oxygen doping composition along the sample length [1], [2]. This method enables us to examine with high resolution the evolving physical properties in the high-temperature superconducting (HTS) compound  $\text{YBa}_2\text{Cu}_3\text{O}_x$  [ $6 \leq x \leq 7$ ]. The process is generally compatible for studies of materials that have a diffusive constituent or interstitial atom or molecule [3]. A sample is initially prepared with a uniform compositional state, e.g., in the case of  $\text{YBa}_2\text{Cu}_3\text{O}_x$  the film is either completely oxygenated or depleted, i.e.,  $x = 6$ , or  $x = 7$ . The film is then placed in an annealing device in which a controlled thermal gradient is established across the longest dimension. The sample is then placed in an atmospherically controlled chamber that is filled to a desired pressure with pure oxygen and the heating device is activated. The heating process is relatively slow, allowing for an equilibrium thermal gradient to be quickly established along the direction of thermal flow and a corresponding continuously varying oxygenation state is formed ( $\text{YBa}_2\text{Cu}_3\text{O}_x \Rightarrow \text{YBa}_2\text{Cu}_3\text{O}_{\nabla x}$ ). See Figure 1. The final distribution of oxygen content along the length of the film can be altered by the additional application of uniaxial pressure to the sample during the annealing process [1], [2], and [4]. In the case of  $\text{YBa}_2\text{Cu}_3\text{O}_{\nabla x}$ , the application of sufficient uniaxial pressure results in the film having discrete regions of uniform oxygen content where  $x \approx [6, 6.5, 6.72, 6.81, 7]$ . See parts (a) and (c) of Figure 2. These oxygen levels correspond to certain known lattice superstructures which have been examined in detail theoretically by de Fontaine et al., and McCormack et al. [5], [6], and [7].

Because the sample preparation method is key to the observation of the pressure stabilized lattice states, we briefly examine and distinguish between the device described in [1], [2], [3], and [4], and that of other gradient annealing devices described by independent authors. Additionally, we examine here fundamental characteristic properties of the lattice superstructures belonging to the superconducting doping region ( $x \geq 6.33$ ). We find that these lattice structures exhibit quantum-like “states” in that they have near integer ratios of the superconducting to normal state carrier densities and condensation energy densities.

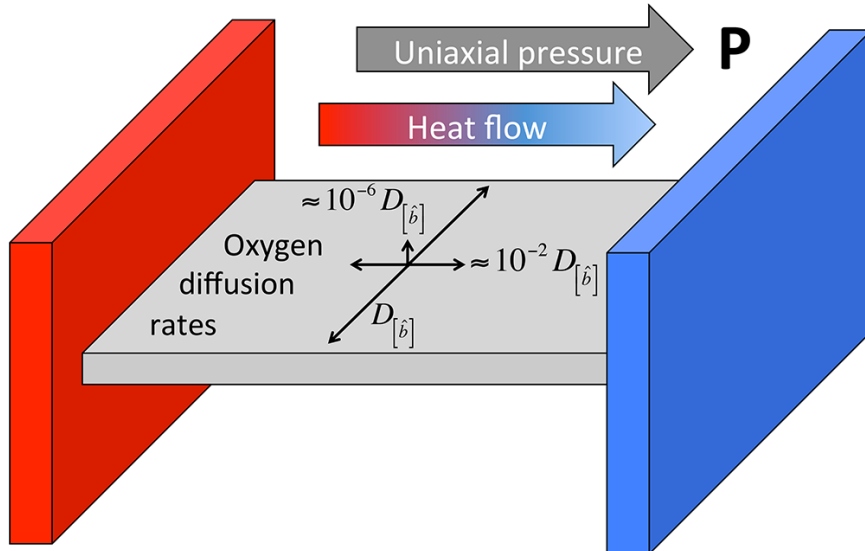


Figure 1. Depiction of the annealing device developed for the preparation of  $\text{YBa}_2\text{Cu}_3\text{O}_{\nabla x}$  films [1] and [3]. The application of pressure results in an alignment of the crystalline a-axis along the direction pressure/thermal gradient. Oxygen diffuses most freely along the b-axis, with minimal mobility along the c-axis which is perpendicular to the film surface/film-substrate boundary. Directional oxygen diffusion rates,  $D$ , relative to the b-axis are indicated.

## 2. GEOMETRY OF THERMAL GRADIENT ANNEALING

The search for new materials and study of known compounds is often facilitated through a systematic doping/substitution of elements within a parent compound. A rapid investigation of the material properties relies on high-throughput production and characterization methods. To enable such a combinatorial materials science approach, the use of gradient annealing devices has been developed by a number of researchers. See references [8]–[16]. In general, these devices are used for rapid optimization of materials in thin film form by the simultaneous processing of a fixed sample composition at different temperatures and/or a stoichiometric variation across the film dimensions, i.e., a chemical gradient that is established during the deposition process. Inherent to the configuration of these devices, the primary component of heat flow from the thermal gradient produced by the heater stage through the supporting substrate and into the film is perpendicular to the surface of the film. In contrast, our design (see Figure 2 (b)) is such that the conduit for the thermal heat path between the heat source and the heat sink (or between two controlled heat sources) is parallel to the substrate/film interface. These devices are routinely used for preparation of metallic samples that have high thermal conductivity and are thermally isotropic, i.e., heat flows the same in all directions.

The compound  $\text{YBa}_2\text{Cu}_3\text{O}_x$  has anisotropic thermal conductivity—near  $x = 7$ , heat flows  $\sim 10$  times greater in the in-plane ( $a - b$ ) direction than in the out of plane ( $c$ ) direction [17]–[21]. On top of this, the anisotropy of the heat flow increases as  $x$  decreases—heat flow becomes even more channeled along the direction of the film/substrate interface as the oxygen content is reduced during the annealing process [20]. This results in non-negligible reflection of heat flow at the film/substrate boundary. The anisotropic thermal properties of  $\text{YBa}_2\text{Cu}_3\text{O}_x$  are highly relevant to the thermal gradient annealing process, as it impacts the manner in which heat flows through the sample and across the film/substrate interface. Standard models for thermal boundary conductance are inadequate to describe heat flow in layered and chainlike materials [22] such as  $\text{YBa}_2\text{Cu}_3\text{O}_x$ . Significantly different results will be obtained depending on whether thermal flow is configured as with our device or is aligned as in References [8]–[15] due to the thermal anisotropy.

A particularly relevant and related subject to the scenarios we are distinguishing between here is that of thermal meta-materials, also referred to as thermal cloaking [23]–[27]. Within this emerging field of study it has been experimentally demonstrated how heat flow can be made to bend through the use of materials having sufficiently different thermal conductivities and tailored anisotropic structures. There are two examples especially relevant to our discussion, (1) a heat waveguide, and (2) a heat spreader.

In Reference [25], Han demonstrates experimentally a new class of metamaterials for use in controlling heat flow, including a thermal concentrator, focusing/resolving, and uniform heating. The devices described by Han are composed of two regular isotropic materials in an optimized geometry which then give rise to a structure having anisotropic thermal properties. See, in particular, Figure 1(b) and (c) of Reference [25] of a schematic depiction wherein heat sources are positioned at the ends of channels created by the alternating of low and high thermally conductive paths and the subsequent controlled directionality of heat flow. See Figures 2–4 of Reference [25] for experimental data demonstrating the concept in action. In Reference [24], Kadic describes various thermodynamic metamaterials, including simple layered materials in planar geometry similar to the film/substrate interface formed by the  $\text{YBa}_2\text{Cu}_3\text{O}_{\nabla x}$  films, and similarly those of Reference [24]. In Reference [27] Dede presents experimental results for heat cloaking, focusing, and reversal in ultra-thin anisotropic composites. All of the preceding examples demonstrate how heat from a source positioned at one end of a structure having a thermal boundary parallel to the primary component of natural heat flow, such as a film as depicted in Figure 2(b), i.e., in the annealing scenario we have developed, heat flows along the direction of the film/substrate interface quite naturally.

Subsequently, the case of what is known as a heat spreader is relevant to the scenario described in References [8]–[16]. An examination of Figure 4 in Reference [25] of the same structure discussed above shows also how heat flow is spread laterally when encountering an anisotropic thermal boundary. Note in particular the inset to Figure 4(c) of Reference [25] where heat flux near the top (and bottom) of the structure that encounters the boundary at an angle close to perpendicular direction is then redirected primarily along the channel formed by the boundary. A second relevant example is that of the extremely anisotropic material graphene [28], [29]. Gao [28] demonstrated the use of graphene layered films as an effective heat spreader. The temperature of a hot spot driven at a heat flux of up to  $430 \text{ W/cm}^2$  was decreased from  $121^\circ\text{C}$  to  $108^\circ\text{C}$  ( $\Delta T \approx 13^\circ\text{C}$ ) with the application of a monolayer of graphene. These examples demonstrate that in an annealing scenario for  $\text{YBa}_2\text{Cu}_3\text{O}_{\nabla_x}$ , wherein heat from the applied thermal gradient must flow through the substrate-film boundary, the thermal lines of flow will be spread out along the film/substrate interface, resulting in a more uniformly heated sample, and subsequently a reduced oxygen gradient along the length of the film.

In the configuration described in References [8]–[16], the interface behaves like a heat-spreader wherein heat flow is spread laterally, resulting more uniform thermal profile and subsequently a reduced variation in the oxygen gradient across the film. In contrast, when the heat/heat sink is applied to the ends of the film, heat flows along the boundary and is effectively channeled like a heat waveguide. See References [24], [25], and [27] for examples of how heat from a source positioned at one end of a structure having a thermal boundary parallel to the primary component of natural heat flow, such as a film as depicted in Figure 2(b), flows along the direction of the film/substrate interface quite naturally. The barrier between the film and substrate acts analogously to that of an optical waveguide. The heat that enters the film primarily stays in the film, and likewise for the substrate. This configuration results in an oxygen profile that is consistent with what is calculated given the controlled annealing conditions (See Figure 2(a)). Without establishing this initial oxygen distribution profile, it is impossible to observe the pressure stabilized lattice states depicted in Figure 2(c) of the hole-doped cuprate  $\text{YBa}_2\text{Cu}_3\text{O}_x$ .

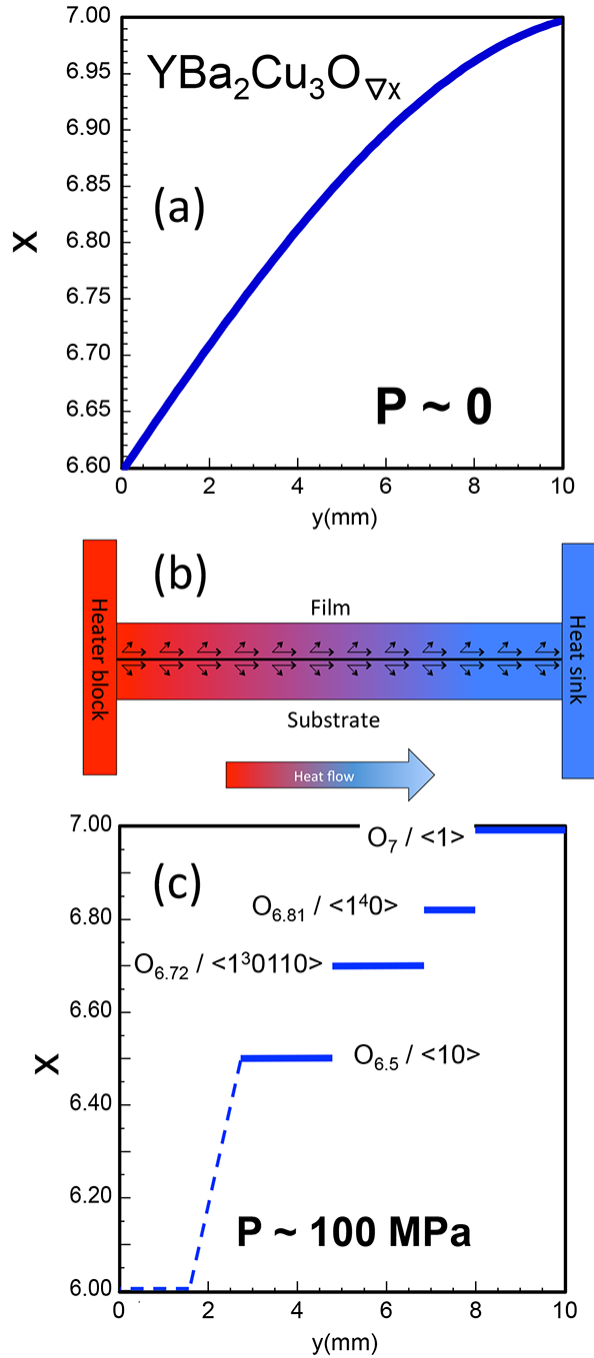


Figure 2. (a) Calculated oxygen distribution along the length of a  $\text{YBa}_2\text{Cu}_3\text{O}_{\nabla x}$  film annealed in a 110-mTorr pure oxygen atmosphere, with the hot end of the film at  $395^\circ\text{C}$  and the cooler end at  $290^\circ\text{C}$ , with zero applied uniaxial mechanical pressure; (b) heat flow in the case of a film having anisotropic thermal conductivity and a large film/substrate thermal boundary resistance where heat is applied along the direction of high thermal conductivity. The heat flow dynamics behave like a thermal cloak device wherein the heat which enters a channel (i.e., film or substrate) largely remains in the channel; (c) calculated oxygen distribution along the length of a  $\text{YBa}_2\text{Cu}_3\text{O}_{\nabla x}$  film annealed in a 110-mTorr pure oxygen atmosphere, with the hot end of the film at  $395^\circ\text{C}$  and the cooler end at  $290^\circ\text{C}$ , with approximately 100 MPa applied uniaxial mechanical pressure.

### **3. FUNDIMENTAL PHYSICAL PROPERTIES OF $\text{YBa}_2\text{Cu}_3\text{O}_x$ vs. HOLE DOPING**

Over the past decade, key experiments have been performed by a number of authors on the evolution of characteristic physical properties of the high- $T_c$  compound  $\text{YBa}_2\text{Cu}_3\text{O}_x$ . By using the reported values of the critical temperature [28],  $T_c$ , the upper critical field [29],  $H_{c2}(0)$ , the superconducting carrier effective mass [30],  $m^*$ , and the superconducting penetration depth [31],  $\lambda$ , we examine the nature of characteristic energy scales of pressure stabilized ‘quantum structural’ lattice states in  $\text{YBa}_2\text{Cu}_3\text{O}_{\nabla_x}$  films. Because the data in the preceding references are not uniformly reported as a function of the same experimental variable, we make particular use of the sets of data given in Reference [28], wherein we have extracted an empirical relationship between the oxygen content,  $x$ , and the hole doping value (in the  $\text{CuO}_2$  planes)  $p(\text{h/Cu})$ , as shown in Figure 3. From this value, we have replotted in Figure 4 the superconducting penetration depth  $\lambda$ , reported in [31] as  $T_c$  vs.  $1/\lambda^2$ , as  $\lambda$  vs.  $p$ . In Figure 5, we have replotted the superconducting carrier effective mass  $m^*$ , reported in [30] as  $m^*$  vs.  $x$ , as  $m^*$  vs.  $p$ . Also shown in both Figures 4 and 5 are empirical fits to the data that are used for the subsequent analysis in Figures 7 and 8.

In Figure 6, we have reproduced the upper critical field data,  $H_{c2}(0)$  vs.  $p$ , from Grissonnanche et al. [29], along with the applied smooth curve fit used for the analysis presented in Figures 7 and 8.

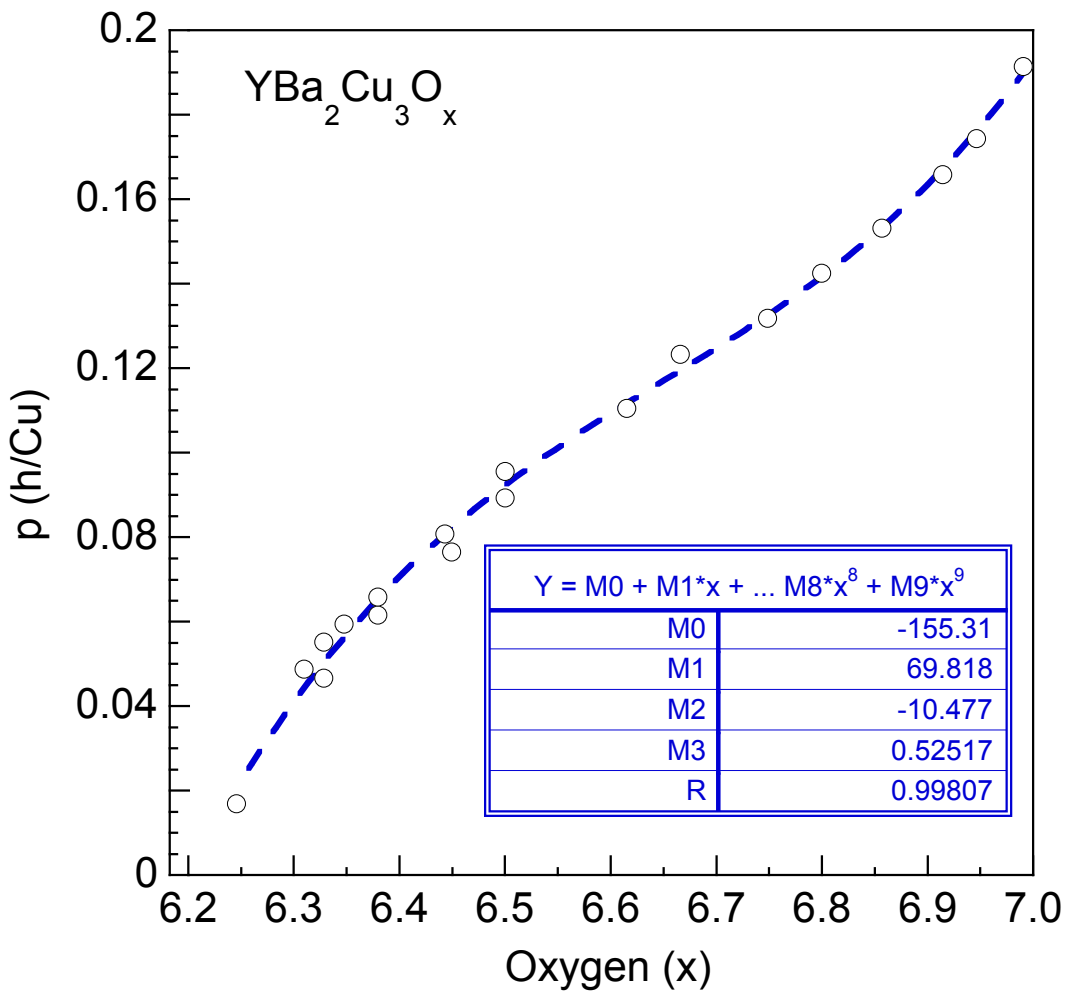


Figure 3. Relationship between the oxygen doping content,  $O_x$ , and the hole doping value,  $p(\text{h/Cu})$ , in the Cu-O<sub>2</sub> planes. The data shown here is produced by combining the data shown in Figures 1 and 2 of Liang, Bonn, and Hardy [28].

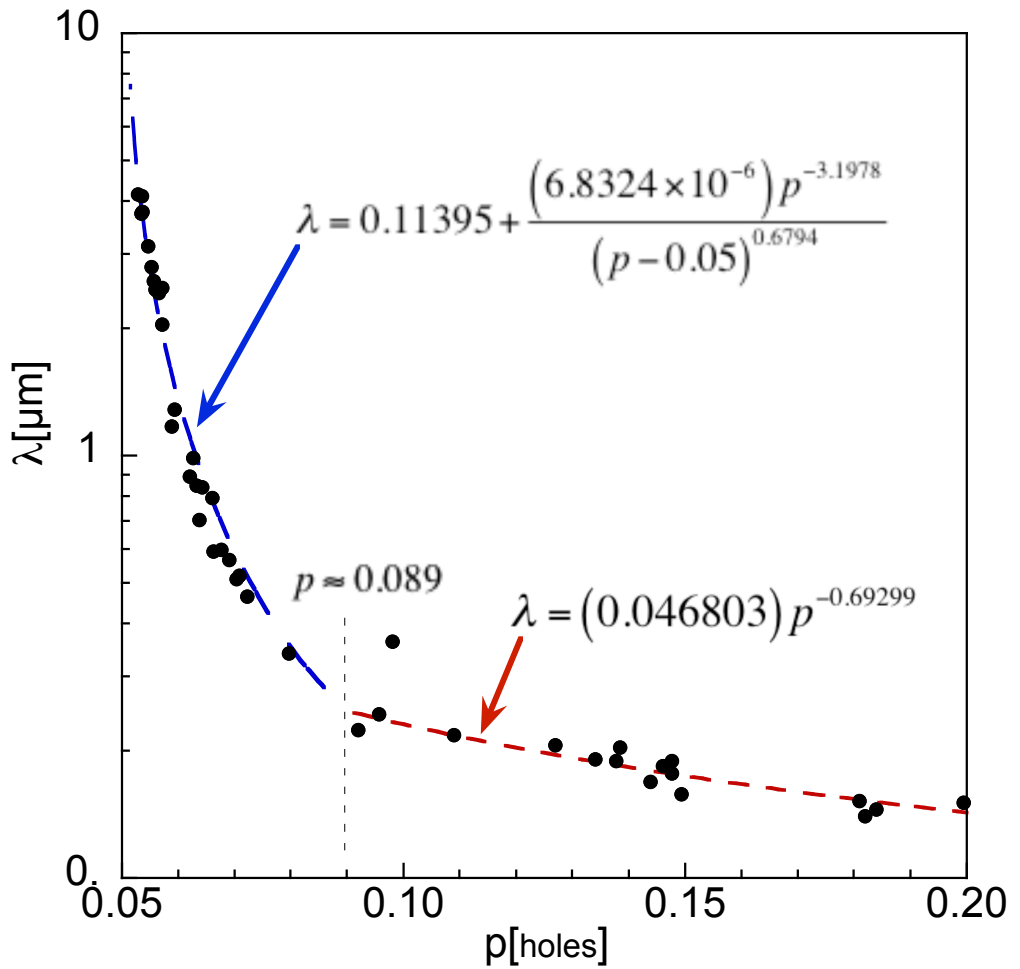


Figure 4. The superconducting penetration depth  $\lambda$  vs.  $p$  of the  $\text{YBa}_2\text{Cu}_3\text{O}_x$  system. Original data was reported by Zuev [33] as  $T_c$  vs.  $1/\lambda^2$ . Also shown are empirical fits to the data for the regions  $p \leq 0.089$  and  $p > 0.089$ . The empirical fits are used for the analysis in Figures 7 and 8.

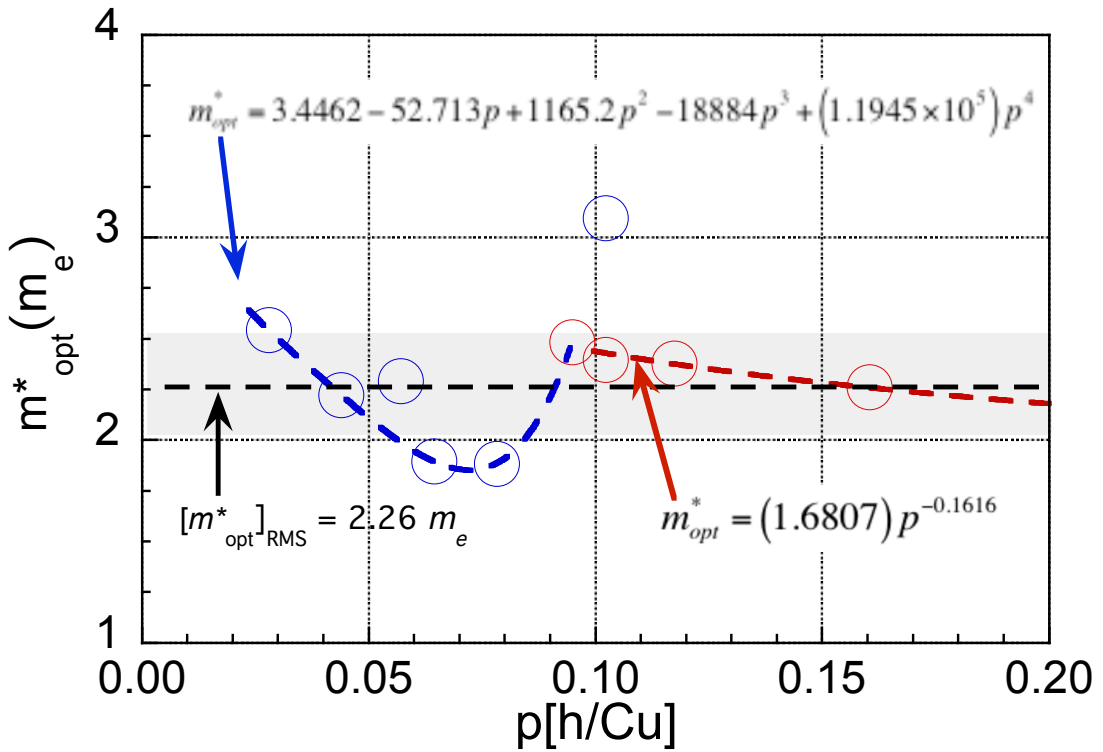


Figure 5. The superconducting effective mass  $m^*$  vs.  $p$  of the  $\text{YBa}_2\text{Cu}_3\text{O}_x$  system as determined from optical conductivity measurements. The original data was reported by [30] as  $m^*$  vs.  $x$ . Also shown are empirical fits to the data for the regions  $p \leq 0.089$  and  $p > 0.089$ . The empirical fits are used for the analysis in Figure 7. We note that the authors interpret the data as indicative of a constant effective mass across the phase diagram. The *rms* value of  $\langle m^* \rangle \approx 2.24 m_e$  is indicated with the black dashed line and the standard deviation of  $\sigma = 0.24 m_e$  is indicated by the shaded region. The single data point with  $m^* \approx 3.1$  was excluded from the *rms* calculation.

## 4. SUPERCONDUCTIVITY AND ORDERED LATTICE STATES

A physical explanation of the electron pairing mechanism in high- $T_c$  cuprate superconductors remains to be established. These materials have a very complex structure—x-ray diffraction studies have shown the existence of lattice modulations [34] which have been explained theoretically by de Fontaine et al. [5], [6] and [7] as having their origin in the ordering of one-dimensional (1-D) O-Cu-O chains located in the CuO planes. Within this model, the 1-D chains are described through a branching algorithm wherein the notation  $\langle 1 \rangle$  and  $\langle 10 \rangle$  denote the Ortho I ( $c = 0.50$ ) and Ortho II ( $c = 0.25$ ) chain states where a one or zero indicates a completely full or empty Cu-O chain, respectively, and an exponent denotes a repeated structure ( $z = 2c + 6$ , where  $z$  is used by the authors to denote the oxygen doping level). Subsequent lower level structures arise from the interspersing, or superposition of higher structures, e.g., the Ortho III structure,  $\langle 110 \rangle = \langle 1 \rangle + \langle 10 \rangle$ , and so forth. These low-temperature ordered oxygen superstructures are stabilized by long-range interactions. More recently, Ricci et al. [35] reported the spatial imaging of oxygen dopant distribution inhomogeneity in  $\text{YBa}_2\text{Cu}_3\text{O}_{6.67}$  via scanning nano X-ray diffraction experiments. The increase of inhomogeneity at the nanoscale is interpreted as evidence for a network of “superconducting puddles” within which oxygen interstitials are well ordered, a result compatible with the above model of de Fontaine et al. [7], wherein the material is composed of the interspersing or superposition of the identified lattice superstructures at oxygen levels in between the corresponding superstructure states.

As noted in Section 1, with the application of sufficient uniaxial pressure to  $\text{YBa}_2\text{Cu}_3\text{O}_{\nabla x}$ , we observed films during the thermal gradient annealing process that discrete regions of uniform oxygen content are stabilized where  $x \approx [6, 6.5, 6.72, 6.81, 7]$ . The latter four oxygen content levels correspond to the lattice superstructures denoted as  $\langle 10 \rangle$ ,  $\langle 1^30110 \rangle$ ,  $\langle 1^40 \rangle$ , and  $\langle 1 \rangle$ , respectively. The concept of a physical superposition of structural states motivates us to further investigate characteristic energy scales associated with the corresponding normal and superconducting states of each lattice structure.

A relationship between the superconducting transition temperature,  $T_c$ , and various well-defined physical properties was found by Taylor and Maple [36]. In one form, the relationship can be written as

$$T_c = \frac{2\pi}{3k_B} \left[ \frac{n_s}{n_n} \right] \left( \frac{\hbar}{\xi_0} \right)^2 \frac{1}{m_s^*}, \quad (1)$$

or equivalently,

$$H_{c2}(0) \approx (0.1776 T/K) \left[ \frac{m_s^*}{m_e} \right] \left[ \frac{n_n}{n_s} \right] T_c, \quad (2)$$

where  $H_{c2}(0) = \Phi_0/2\pi\xi_0^2$  is the upper critical field,  $\xi_0$  is the Cooper pair coherence length,  $m_e$  is the free electron mass,  $m_s^*$  is the superconducting electron mass,  $n_n$  is the normal state charge carrier density, and  $n_s$  is the superconducting state carrier density.

We make use of the superconducting effective mass data,  $m^*$  vs.  $p$ , and the upper critical field data,  $H_{c2}(0)$  vs.  $p$ , shown in Figures 5 and 6, respectively, and the smooth curve fits to the critical temperature data,  $T_c$  vs.  $p$  of Liang, Bonn, and Hardy [30], to calculate the ratio of the normal state carrier density to the superconducting state carrier density,  $\frac{n_n}{n_s}$ . The value of  $\frac{n_n}{n_s} < 1$  is not possible, and hence the calculated value reflects some of the error inherent to the reported values of the data in Figures 3–6. However, we observe the interesting result that the stabilized lattice superstructures belonging to the superconducting doping region ( $x \geq 6.33$ ) have near integer ratios of  $[n_n/n_s]$ , a result that is consistent with quantized energy levels of the stabilized lattice superstructures. Next, in Figure 8 we use the upper critical field data in Figure 6 and the superconducting penetration depth data shown in Figure 4 to calculate the condensation energy density as a function of hole doping normalized to the lowest point in the region  $0.089 < p < 0.20$ ,

i.e., in the doping range over which the superlattice states are formed. Here we notice that the ratios of the condensation energy densities of the first two (stabilized fourth level) states,  $\langle 10 \rangle$  and  $\langle 1^30110 \rangle$ , have near equal values and the values of the ratios of the condensation energy densities of the last two lattice states,  $\langle 1^40 \rangle$  and  $\langle 1 \rangle$ , are a factor of 2 and 7 larger. This result is also suggestive of a quantization of the energy levels associated with the superconducting mechanism in each superlattice structure, and hence superconductivity in the regions (oxygen/hole doping levels) between are a superposition of the (structural) ground states.

Given that Equation (1) does not invoke any particular superconducting mechanism, it then provides a framework into which results of a specific theory of superconductivity involving the characteristic physical properties ( $n_s/n_n$ ),  $\xi_0$ , and  $m_s^*$ , can be inserted. We now examine the relationship between the expression for  $T_c$  given here, and that found in the BCS-Eliashberg theory of superconductivity by inserting the BCS (s-wave) definition of the coherence length [37],  $\xi_0 = \hbar v_F / \pi \Delta_0$ , into Equation (1). While it is customary to use values of the Fermi velocity  $v_F$  obtained via measurements of normal state properties in the above expression, just as we did above for the effective electron mass, we specify a Fermi velocity associated with the superconducting state,  $v_{Fs}$ . This distinction is an acknowledgment of the fact that the kinetic energy of the electrons,  $m^*v_F^2/2$ , changes upon entering the superconducting state. It is well established that the electronic kinetic energy increases in conventional superconductors [37] and [38], and there is growing experimental and theoretical evidence that in the high- $T_c$  cuprates there is a reduction of the electronic kinetic energy [39], [40], [41], and [42]. Then, with this change of notation, by inserting  $\xi_0$  (BCS) into Equation (2), we find

$$T_c = \frac{\pi^3}{3k_B} \left( \frac{n_s}{n_n} \right) \frac{\Delta_0^2}{\frac{1}{2} m_s^* v_{Fs}^2}. \quad (3)$$

We can, of course, rearrange Equation (3) to take the recognizable BCS-Eliashberg form,

$$2\Delta_0 = \eta k_B T_c,$$

where  $\eta$  is the coupling constant, such that

$$\eta \equiv \frac{6}{\pi^3} \left( \frac{n_n}{n_s} \right) \frac{\frac{1}{2} m_s^* v_{Fs}^2}{\Delta_0}. \quad (4)$$

Rearranging Equation (4) gives

$$\left( \frac{n_n}{n_s} \right) = \eta \frac{\pi^3}{6} \frac{\Delta_0}{\frac{1}{2} m_s^* v_{Fs}^2}, \quad (5)$$

so we can observe from Figure 7 the relative changes between the product of the strength of the coupling mechanism with the ratio of the gap energy to the superconducting electron kinetic energy. The near integer increments of the values of  $n_n/n_s$  associated with the superlattice oxygen levels highlights the likely fundamental quantum nature of the superstructure lattice states. While not conclusive, this observed relationship suggests that the relationship between superconductivity and the lattice structure merits further investigation from the perspective of quantum structural states.

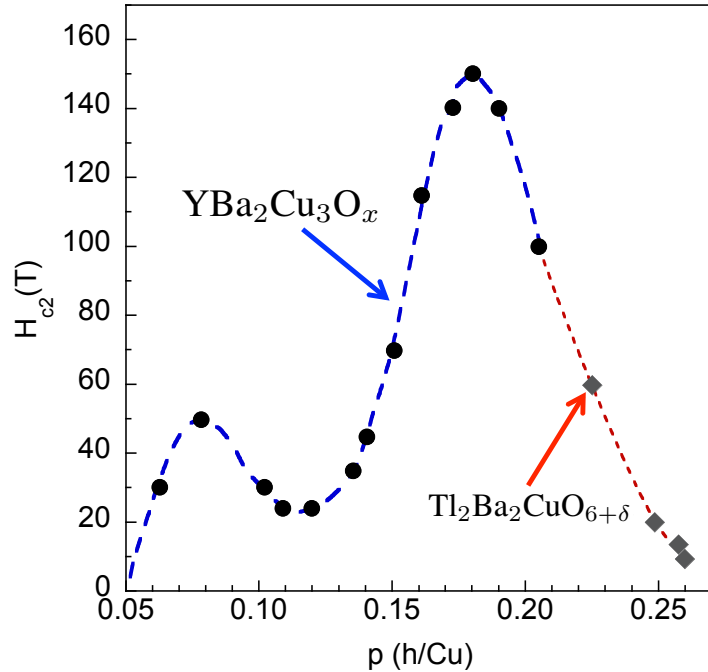


Figure 6. Upper critical field,  $H_{c2}(0)$ , of the hole-doped cuprates  $\text{YBa}_2\text{Cu}_3\text{O}_x$  and  $\text{Tl}_2\text{Ba}_2\text{CuO}_{6+\delta}$ . Data is reproduced from Grisonnaud et al. [29]. The blue dashed line indicates the curve fit to the  $\text{YBa}_2\text{Cu}_3\text{O}_x$  upper critical field data that is used for subsequent analysis. The red dashed line is a smooth fit to the upper critical field data of  $\text{Tl}_2\text{Ba}_2\text{CuO}_{6+\delta}$ , for continuity.

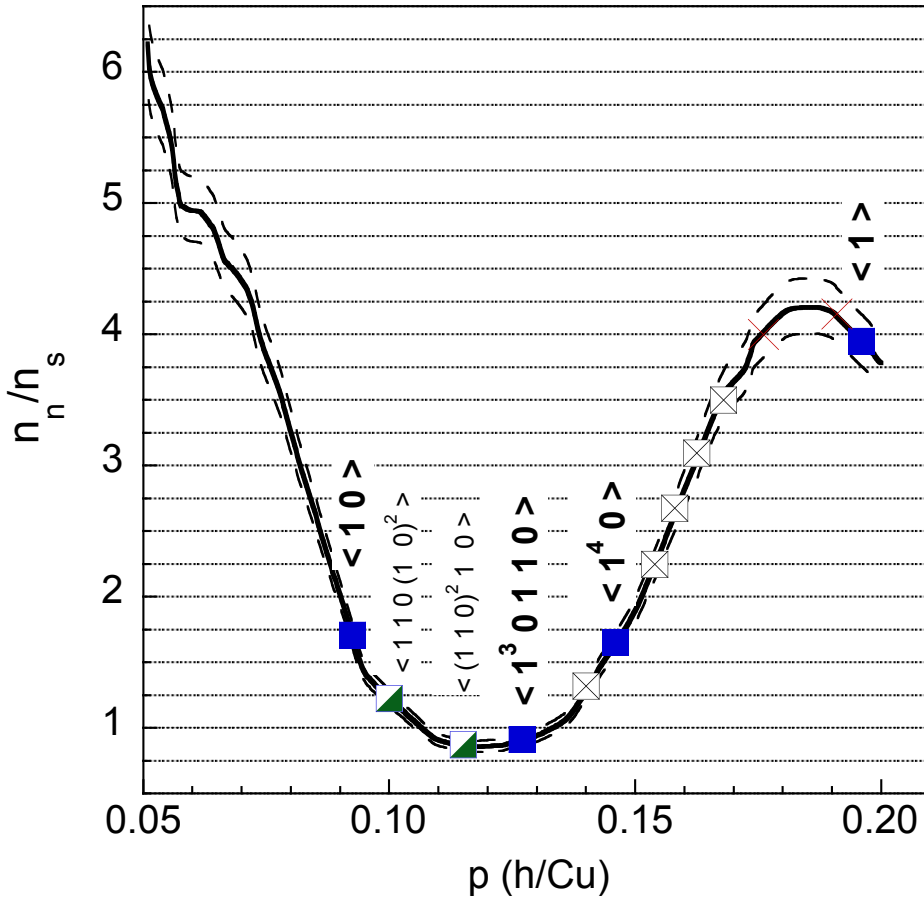


Figure 7. Calculated ratio of the normal state carrier density to the superconducting state carrier density  $\frac{n_n}{n_s}$  vs.  $p$  for the  $\text{YBa}_2\text{Cu}_3\text{O}_x$  system. The values shown were calculated as described in the text. The dashed lines are calculated by assuming a  $\pm 0.2 m_e$  deviation of  $m^*$ . The corresponding locations of the superstructure lattice states are indicated. Filled squares correspond to pressure stabilized fourth level branch states as described by [5]; open squares with filled triangles indicate metastable fourth level states; open squares with  $\times$  indicate possible locations of lower level branches; Red  $\times$  indicates the absence of any predicted state.

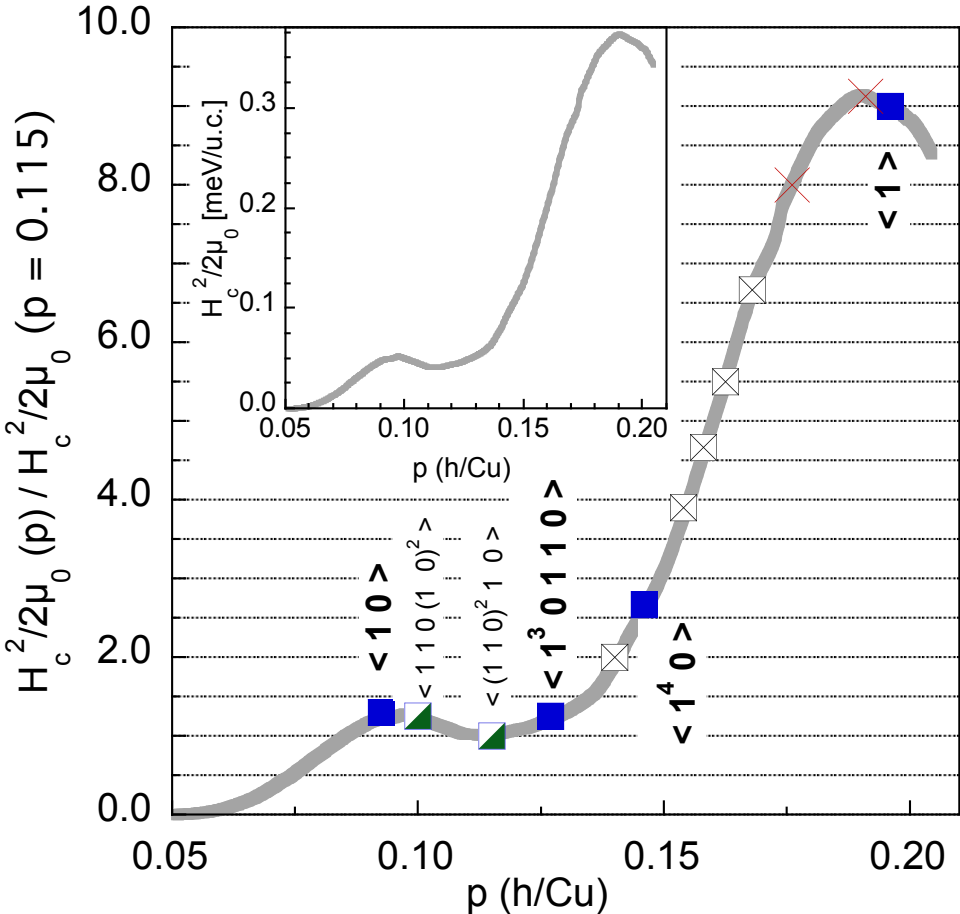


Figure 8. Normalized value of condensation energy density as a function of hole doping,  $\frac{H_c^2(0)}{2\mu_0}(p) / \frac{H_c^2(0)}{2\mu_0}(p = 0.115)$  vs.  $p[h]$ , in the compound  $\text{YBa}_2\text{Cu}_3\text{O}_x$ . The corresponding locations of the superstructure lattice states are indicated: filled squares correspond to pressure stabilized fourth level branch states as described by [5]; open squares with filled triangles indicate metastable fourth level states; open squares with  $\times$  indicates possible locations of lower level branches; Red  $\times$  indicates the absence of any predicted state. The inset shown the unnormalized calculated value of the condensation energy density,  $\frac{H_c^2(0)}{2\mu_0}(p)$ , in units of meV per lattice unit cell. The unit cell dimensions are taken as a constant with oxygen doping as  $a \times b \times c = (3.823\text{\AA})(3.885\text{\AA})(11.68\text{\AA})$ .

## 5. CONCLUSION

We discuss here the importance of the configuration of heat flow in establishing a well-controlled, high-quality  $\text{YBa}_2\text{Cu}_3\text{O}_{\nabla x}$  film sample. The anisotropic thermal conductivity of  $\text{YBa}_2\text{Cu}_3\text{O}_x$  plays a critical role in the final compositional spread of oxygen content. A  $\text{YBa}_2\text{Cu}_3\text{O}_x$  film annealed with a device wherein the heat must flow through the substrate/film interface will result in a poorly controlled oxygen concentration gradient. In contrast, by employing a geometry such that the film and substrate are parallel thermal conduits, we have successfully demonstrated  $\text{YBa}_2\text{Cu}_3\text{O}_{\nabla x}$  films having a well-controlled oxygen concentration gradient that fully spans the range expected from the known thermodynamic relationship between temperature, atmospheric pressure, and dopant (oxygen) concentration [41].

Finally, by using values from the literature, we have examined the evolution of associated energy levels of the stabilized lattice states  $<10>$ ,  $<1^30110>$ ,  $<1^40>$ , and  $<1>$ , and find evidence for discrete energy levels of the pressure stabilized lattice superstructures.

## REFERENCES

1. B. J. Taylor, C. A. McElroy, I. K. Lum, A. M. Leese de Escobar, M. C. de Andrade, T. J. Wong, E. Y. Cho, and M. B. Maple. 2015. “Correlation of Structural, Magnetic, and Electronic Transitions of a Novel Charge-gradient  $\text{YBa}_2\text{Cu}_3\text{O}_{\text{v}_x}$  Film,” *Physical Review B*, vol. 91, pp. 144511:1–12.
2. B. J. Taylor, T. H. Emery, S. A. E. Berggren, A. M. L. de Escobar, J. Inho, and M. B. Maple. 2015. “Preparation of Novel HTS Films and Tunnel Junctions for Advanced C3I Sensor Applications.” *Proceedings of the SPIE* Volume 9467 (pp. 946725:1–11). G. Thomas, D. K. Achyut, and M. S. Islam, Eds. April 20–24, Baltimore, MD.
3. B. J. Taylor. “System and Method for Producing a Sample Having a Monotonic Doping Gradient of a Diffusive Constituent or Interstitial Atom or Molecule.” U.S. Patent 9,188,514 B1 filed May 23, 2013, and issued November 17, 2015.
4. B. J. Taylor. 2016. “Apparatus and Methods for Production of Untwinned YBCO Films.” Filed December 1, 2014. U.S. Patent Pending.
5. D. de Fontaine, G. Cedar, and M. Asta. 1990 “Low-temperature Long-range Oxygen Order in  $\text{YBa}_2\text{Cu}_3\text{O}_z$ ,” *Nature*, vol. 343, pp. 544–546.
6. R. McCormack, and D. de Fontaine. 1992 “Oxygen Configurations and Their Effect on Charge Transfer in Off-stoichiometric  $\text{YBa}_2\text{Cu}_3\text{O}_z$ ,” *Physical Review B*, vol. 45, pp. 12976–12987.
7. D. de Fontaine, V. Ozolins, Z. Islam, and S. C. Moss. 2005 “Origin of Modulated Structures in  $\text{YBa}_2\text{Cu}_3\text{O}_{6.63}$ : A First-principles Approach,” *Physical Review B*, vol. 71, pp. 212504:1–4.
8. A. Tsukazaki, H. Saito, K. Tamura, and M. Kawasaki. 2002. “Systematic Examination of Carrier Polarity in Composition Spread ZnO Thin Films Codoped with Ga and N,” *Applied Physics Letters*, vol. 81, pp. 235–237.
9. T. Koida, D. Komiyama, H. Koinuma, M. Ohtani, M. Lippmaa, and M. Kawasaki. 2002. “Temperature-gradient Epitaxy Under in situ Growth Mode Diagnostics by Scanning Reflection High-energy Electron Diffraction,” *Applied Physics Letters*, vol. 80, pp. 565–567.
10. H. Minami, K. Itaka, P. Ahmet, D. Komiyama, T. Chikyow, M. Lippmaa, and H. Koinuma. 2002. “Rapid Synthesis and Scanning Probe Analysis of  $\text{Ba}_x\text{Sr}_{1-x}\text{TiO}_3$  Composition Spread Films on a Temperature Gradient Si (100) Substrate,” *Japanese Journal of Applied Physics*, vol. 41, pp. L149–L151.
11. T. Koida, T. Wakisaka, K. Itaka, and Y. Matsumoto. 2002. “Metal-insulator-metal Transition in  $\text{Sr}_2\text{Rh}_{1-x}\text{Ru}_x\text{O}_4$  ( $0 \leq x \leq 1$ )”, *Applied Physics Letters*, vol. 8, pp. 4955–4957.
12. J. Nishimura, T. Fukumura, M. Ohtani, Y. Taguchi, M. Kawasaki, I. Ohkubo, H. Koinuma, H. Ohguchi, K. Ono, M. Oshima, and Y. Tokura. 2003. “Fabrication of Spin-frustrated  $\text{Sm}_2\text{Mo}_2\text{O}_7$  Epitaxial Films: High Throughput Optimization Using a Temperature Gradient Method,” *Applied Physics Letters*, vol. 82, pp. 1571–1573.

13. T. Wakisaka, T. Koida, Y. Matsumoto, K. Itaka, and H. Koinuma. 2004. “Sr<sub>2</sub>Rh<sub>1-x</sub>Ru<sub>x</sub>O<sub>4</sub> (0 ≤ x ≤ 1), Composition-spread film Growth on a Temperature-gradient Substrate by Pulsed Laser Deposition,” *Applied Surface Science*, vol. 223, pp. 264–267.
14. Y. Yamada, T. Fukumura, M. Ikeda, M. Ohtani, H. Toyosaki, A. Ohtomo, F. Matsukura, H. Ohno, and M. Kawasaki. 2005. “Fabrication of Ternary Phase Composition - Spread Thin Film Libraries and Their High-Throughput Characterization: Ti<sub>1-x-y</sub>Zr<sub>x</sub>Hf<sub>y</sub>O<sub>2</sub> for Bandgap Engineering,” *Journal of Superconductivity and Novel Magnetism*, vol. 18, pp. 109–113.
15. S. Thienhaus, R. Hhiergeist, A. Savan, and A. Ludwig. 2006. “Design and Application of Gradient Annealing Devices for the Parallel Thermal Processing of Fe/Pt Multilayers,” *Materials Research Society Bulletin Library*, vol. 894, pp. 0984-LL01-04.1.
16. S. Okazaki, N. Biruajum, F. Yasushi, H. Yutaka, S. Taro, and T. Hasegawa. 2006. “High-throughput Characterization of Local Conductivity of Nd<sub>0.9</sub>Ca<sub>0.1</sub>Ba<sub>2</sub>Cu<sub>3</sub>O<sub>7-8</sub> Thin Film by the Low-temperature Scanning Microwave Microscope,” *Applied Surface Sciences*, vol. 252, pp. 2615–2621.
17. S. J. Hagen, Z. Z. Wang, and N. P. Ong. 1989. “Anisotropy of the Thermal Conductivity of YBa<sub>2</sub>Cu<sub>3</sub>O<sub>7-y</sub>,” *Physical Review B*, vol. 40, pp. 9389–9392.
18. A. Bock. 1995. “Laser Heating of YBa<sub>2</sub>Cu<sub>3</sub>O<sub>7</sub> Films in Raman Experiments,” *Physical Review B*, vol. 51, pp. 15506–15518.
19. M. Matsukawa, T. Mizukoshi, K. Noto, and Y. Shiohara. 1996. “In-plane and Out-of-plane Thermal Conductivity of a Large Single Crystal of YBa<sub>2</sub>Cu<sub>3</sub>O<sub>7-x</sub>,” *Physical Review B*, vol. 53, pp. R6034–R6037.
20. A. V. Inyushkin, A. N. Taldenkov, and T. G. Uvarova. 1996. “Thermal Conductivity of Oxygen-deficient YBa<sub>2</sub>Cu<sub>3</sub>O<sub>6+x</sub>” *Physical Review B*, vol. 54, pp. 13261–13268.
21. T. Ikeda, T. Ando, Y. Taguchi, and Y. Nagasaka. 2013. “Size Effect of Out-of-plane Thermal Conductivity of Epitaxial YBa<sub>2</sub>Cu<sub>3</sub>O<sub>7-8</sub> Thin Films at Room Temperature Measured by Photothermal Radiometry,” *Journal of Applied Physics*, vol. 113, pp. 183517:1–7.
22. Z. Chen, Z. Wei, Y. Chen, and C. Dames. 2013. “Anisotropic Debye Model for the Thermal Boundary Conductance,” *Physical Review B*, vol. 87, pp. 125426:1–14.
23. R. Schittny, M. Kadic, S. Guenneau, and M. Wegener. 2013. “Experiments on Transformation Thermodynamics: Molding the Flow of Heat,” *Physical Review Letters*, vol. 110, pp. 195901:1–5.
24. M. Kadic, T. Buckmann, R. Schittny, and M. Wegener. 2013. “Metamaterials Beyond Electromagnetism,” *Reports on Progress in Physics*, vol. 76, pp. 126501:1–34.
25. T. Han, X. Bai, D. Liu, D. Gao, B. Li, J. T. Thong, and C. W. Qui. 2015. “Manipulating Steady Heat Conduction by Sensushaped Thermal Metamaterials,” *Scientific Reports*, vol. 5, pp. 10242:1–7.
26. F. Chen, and D. Y. Lei. 2015. “Experimental Realization of Extreme Heat Flux Concentration with 2 Easy-to-make Thermal Metamaterials,” *Scientific Reports*, vol. 5, pp. 11552:1–7.

27. E. M. Dede, T. Nomura, P. Schmalenberg, and J. S. Lee. 2013. "Heat Flux Cloaking, Focusing, and Reversal in Ultra-thin Composites Considering Conduction-convection Effects," *Applied Physics Letters*, vol. 103, pp. 063501:1–4.
28. Z. Gao, Y. Zhang, Y. Fud, Matthew M. F. Yuenb, and J. Liua. 2013. "Thermal Chemical Vapor Deposition Grown Graphene Heat Spreader for Thermal Management of Hot Spots," *CARBON*, vol. 61, pp. 342–348.
29. E. Pop, V. Varshney, and A. K. Roy. 2012. "Thermal Properties of Graphene: Fundamentals and Applications," *Materials Research Society Bulletin*, vol. 37, pp. 1273–1281.
30. R. D. Liang, A. Bonn, and W. N. Hardy. 2006. "Evaluation of CuO<sub>2</sub> Plane Hole Doping in YBa<sub>2</sub>Cu<sub>3</sub>O<sub>6+x</sub> Single Crystals," *Physical Review B*, vol. 73, pp. 18505(R):1–4.
31. G. Grissonnanche, O. Cyr-Choinière, F. Laliberté, S. René de Cotret, A. Juneau-Fecteau, S. Dufour-Beauséjour, M. È. Delage, D. LeBoeuf, J. Chang, B. J. Ramshaw, D. A. Bonn, W. N. Hardy, R. Liang, S. Adachi, N. E. Hussey, B. Vignolle, C. Proust, M. Sutherland, S. Krämer, J. H. Park, D. Graf, N. Doiron-Leyraud, and Louis Taillefer. 2014. "Direct Measurement of the Upper Critical Field in Cuprate Superconductors," *Nature Communications*, vol. 5, pp. 3280:1–8.
32. W. J. Padilla, Y. S. Lee, M. Dumm, G. Blumberg, S. Ono, Kouji Segawa, Seiki Komiya, and Yoichi Ando, and D. N. Basov. 2005. "Constant Effective Mass across the Phase Diagram of High-Tc Cuprates," *Physical Review B*, vol. 72, pp. 060511(R):1–4.
33. Y. Zuev, M. S. Kim, and T. R. Lemberger. 2005. "Correlation Between Superfluid Density and Tc of Underdoped YBa<sub>2</sub>Cu<sub>3</sub>O<sub>6+x</sub> Near the Superconductor-insulator Transition," *Physical Review Letters*, vol. 95, pp. 137002:1–4.
34. Z. Islam, S. K. Sinha, D. Haskel, J. C. Lang, G. Srayer, B. W. Veal, D. R. Haeffner, and H. A. Mook. 2002. "X-ray Diffraction Study of Lattice Modulations in an Underdoped YBa<sub>2</sub>Cu<sub>3</sub>O<sub>6+x</sub> Superconductor," *Physical Review B*, vol. 66, pp. 092501:1–4.
35. A. Ricci, N. Poccia, G. Campi, F. Coneri, A. S. Caporale, D. Innocenti, M. Burghammer, M. V. Zimmermann, and A. Bianconi. 2013. "Multiscale Distribution of Oxygen Puddles in One-eighth Doped YBa<sub>2</sub>Cu<sub>3</sub>O<sub>6.67</sub>," *Scientific Reports*, vol. 3, pp. 2383:1–4.
36. B. J. Taylor, and M. B. Maple. 2009. "Formula for the Critical Temperature of Superconductors Based on the Electronic Density of States and the Effective Mass," *Physical Review Letters*, vol. 102, pp. 137003:1–4.
37. J. Bardeen, L. N. Cooper, and J. R. Schrieffer. 1957. "Theory of Superconductivity," *Physical Review*, vol. 108, pp. 1175–1204.
38. G. V. Chester. 1956. "Difference between Normal and Superconducting States of a Metal," *Physical Review*, vol. 103, pp. 1693–1699.
39. A. S. Katz, S. I. Woods, E. J. Singley, T. W. Li, M. Xu, D. G. Hinks, R. C. Dynes, and D. N. Basov. 2000. "Interlayer Conductivity in the Superconductor Tl<sub>2</sub>Ba<sub>2</sub>CuO<sub>6+δ</sub>: Energetics and Energy Scales," *Physical Review B*, vol. 61, pp. 5930–5933.
40. G. Deutscher, A. F. Santander-Syro, and N. Bontemps. 2005. "Kinetic Energy Change with Doping Upon Superfluid Condensation in High-temperature Superconductors," *Physical Review B*, vol. 72, pp. 092504:1–3.

41. T. Eckl, W. Hanke, and E. Arrigoni. 2003. “Phase-fluctuation-induced Reduction of the Kinetic Energy at the Superconducting Transition,” *Physical Review B*, vol. 68, pp. 014505:1–5.
42. T. A. Maier, M. Jarrell, A. Macridin, and C. Slezak. 2004 “Kinetic Energy Driven Pairing in Cuprate Superconductors,” *Physical Review Letters*, vol. 92, pp. 027005:1–4.
43. T. B. Lindemer, J. F. Hunley, J. E. Gates, A. L. Sutton JR., J. Brynestad, C. R. Hubbard, and P. K. Gallageher. 1989. “Experimental and Thermodynamic Study of Non-stoichiometry in  $\text{YBa}_2\text{Cu}_3\text{O}_{7-x}$ ,” *Journal of the American Ceramic Society*, vol. 72, pp. 1775–1788.

REPORT DOCUMENTATION PAGE					Form Approved OMB No. 0704-0188
<p>The public reporting burden for this collection of information is estimated to average 1 hour per response, including the time for reviewing instructions, searching existing data sources, gathering and maintaining the data needed, and completing and reviewing the collection of information. Send comments regarding this burden estimate or any other aspect of this collection of information, including suggestions for reducing the burden to Department of Defense, Washington Headquarters Services Directorate for Information Operations and Reports (0704-0188), 1215 Jefferson Davis Highway, Suite 1204, Arlington VA 22202-4302. Respondents should be aware that notwithstanding any other provision of law, no person shall be subject to any penalty for failing to comply with a collection of information if it does not display a currently valid OMB control number.</p> <p><b>PLEASE DO NOT RETURN YOUR FORM TO THE ABOVE ADDRESS.</b></p>					
1. REPORT DATE (DD-MM-YYYY) March 2017		2. REPORT TYPE Final		3. DATES COVERED (From - To)	
4. TITLE AND SUBTITLE  Evaluation of Characteristic Energy Scales of Pressure Stabilized Oxygen Chain States in YBa <sub>2</sub> Cu <sub>3</sub> O <sub>v</sub> <sub>x</sub> films				5a. CONTRACT NUMBER	
				5b. GRANT NUMBER	
				5c. PROGRAM ELEMENT NUMBER	
6. AUTHORS  Benjamin J. Taylor Teresa Emery-Adleman				5d. PROJECT NUMBER	
				5e. TASK NUMBER	
				5f. WORK UNIT NUMBER	
7. PERFORMING ORGANIZATION NAME(S) AND ADDRESS(ES)  SSC Pacific 53560 Hull Street San Diego, CA 92152-5001				8. PERFORMING ORGANIZATION REPORT NUMBER  TR 3060	
9. SPONSORING/MONITORING AGENCY NAME(S) AND ADDRESS(ES)  SSC Pacific 53560 Hull Street San Diego, CA 92152-5001				10. SPONSOR/MONITOR'S ACRONYM(S) SSC Pacific	
				11. SPONSOR/MONITOR'S REPORT NUMBER(S)	
12. DISTRIBUTION/AVAILABILITY STATEMENT  Approved for public release.					
13. SUPPLEMENTARY NOTES  This is work of the United States Government and therefore is not copyrighted. This work may be copied and disseminated without restriction.					
14. ABSTRACT  Over the past decade key experiments have been performed by a number of authors on the evolution of characteristic physical properties of the high-T <sub>c</sub> compound YBa <sub>2</sub> Cu <sub>3</sub> O <sub>x</sub> . By using the now available reported values of the critical temperature, T <sub>c</sub> , the upper critical field, H <sub>c2</sub> (0), the superconducting effective mass, m*, and the superconducting penetration depth, λ, we examine the nature of characteristic energy scales of pressure stabilized “quantum structura” lattice states in YBa <sub>2</sub> Cu <sub>3</sub> O <sub>v</sub> <sub>x</sub> films. The report shows the importance of the configuration of heat flow in establishing a well-controlled, high-quality YBa <sub>2</sub> Cu <sub>3</sub> O <sub>v</sub> <sub>x</sub> film sample. Additionally discussed is the anisotropic thermal conductivity of YBa <sub>2</sub> Cu <sub>3</sub> O <sub>x</sub> plays a critical role in the final compositional spread of oxygen content. A YBa <sub>2</sub> Cu <sub>3</sub> O <sub>x</sub> film annealed with a device wherein the heat must flow through the substrate/film interface will result in a poorly controlled oxygen concentration gradient. In contrast, by employing a geometry such that the film and substrate are parallel thermal conduits. This report demonstrates YBa <sub>2</sub> Cu <sub>3</sub> O <sub>v</sub> <sub>x</sub> films having a well-controlled oxygen concentration gradient that fully spans the range expected from the known thermodynamic relationship between temperature, atmospheric pressure, and dopant (oxygen) concentration. Finally, by using values from the literature, this report examines the evolution of associated energy levels of the stabilized lattice states <10>, <1 <sup>3</sup> 0110>, <1 <sup>4</sup> 0>, and <1>, and find evidence for discrete energy levels of the pressure stabilized lattice superstructures.					
15. SUBJECT TERMS  annealing device; lattice superstructures; film oxygen content; systemic doping/substitution; substrate/film interface; thermal conductivity; heat waveguide; heat spreader; YBa <sub>2</sub> Cu <sub>3</sub> O <sub>v</sub> <sub>x</sub> films; pressure stabilized oxygen chain states					
16. SECURITY CLASSIFICATION OF:  a. REPORT U		17. LIMITATION OF ABSTRACT  b. ABSTRACT U		18. NUMBER OF PAGES  c. THIS PAGE U	19a. NAME OF RESPONSIBLE PERSON Benjamin J. Taylor
				25	19B. TELEPHONE NUMBER (Include area code) 619-553-4905

## **INITIAL DISTRIBUTION**

84300	Library	(1)
71730	B. Taylor	(1)
71730	T. Emery-Adleman	(1)

Defense Technical Information Center  
Fort Belvoir, VA 22060-6218 (1)

Approved for public release.

**SPAWAR**



*Systems Center  
PACIFIC*



SSC Pacific  
San Diego, CA 92152-5001